

Calibration of Mie Scattering Imaging for microbubble measurement in hydrodynamic test facilities

Patrick Russell · James Venning · Bryce W. Pearce · Paul A. Brandner

Received: DD Month YEAR / Accepted: DD Month YEAR

Abstract Calibration of the Mie Scattering Imaging (MSI) technique for microbubble size and concentration measurement in hydrodynamic test facilities is investigated. Monodisperse bubbles are generated by a microfluidic ‘T’ junction, and individual bubbles simultaneously imaged with shadowgraphy and MSI. Nominal bubble diameters between 30 and 150 μm were tested. The influence of fringe uniformity and intensity for each polarisation on measurement precision was investigated. Parallel polarisation was chosen over perpendicular for its more uniform spacing despite the lower intensity. The linear relation between fringe wavelength and bubble diameter was demonstrated at a measurement angle of 90° . The calibration was derived from constants for light scattering, and for the imaging optics. The wavelength of the scattered fringe pattern is predicted using the Lorentz-Mie theory. A practical method for the calibration of interference patterns is presented. Using this approach the measured bubble diameters from the shadowgraphy and MSI compare to within 1 μm . A method for determining the size dependent measurement volume for axisymmetric and arbitrary beam profiles is also presented.

Keywords Mie Scattering Imaging · Interferometric Mie Imaging · Cavitation · Microbubble Measurement

1 Introduction

On the macroscopic scale almost all volumes of water of practical interest contain bubbles. However, the range of sizes and concentrations present varies greatly. For breaking ocean waves the spectrum of bubble radii extends at least four decades, with bubble concentrations found across six decades (Deane and Stokes, 2002). Most bubble measurement techniques lack the dynamic range to measure across one of these parameters, let alone both, therefore hydrodynamic test facilities require multiple techniques in order to cover the full gamut of possibilities (Brandner, 2018). Mechanical techniques often cover a larger dynamic range but are inherently intrusive to implement (Venning et al., 2018; Chahine and Kalumuck, 2003). Optical techniques are non-intrusive but are usually restricted to approximately two decades in either the concentration, size, or both (Xu, 2001; Randolph et al., 2014). In addition, these techniques have a lower limit which is of the order of the wavelength of light used. Exceptions to this, most notably holography, typically require a high level of rigour to accomplish (Katz and Sheng, 2010). Mie Scattering Imaging (MSI) is an important technique as it covers a difficult region of the size-concentration map, being able to measure bubbles on the order of micrometers in size at very low concentrations. The technique has been given many names including: Interferometric Laser Imaging (Glover et al., 1995), Mie Scattering Imaging (Dunker et al., 2016), Global Phase Doppler (Damaschke et al., 2002; Albrecht et al., 2013), Interferometric Laser Imaging for Droplet Sizing (Glover et al., 1995), and Interferometric Particle Imaging (Ebert et al., 2014). The general principle by which these methods operate is the same, monochromatic light illuminates a transparent bubble (or particle) and the light scattered from it produces an

P. Russell
University of Tasmania
E-mail: patrick.russell@utas.edu.au

J. Venning
University of Tasmania

interference pattern. The frequency of this interference pattern can be mapped to the bubble size.

These interference patterns can be captured using out-of-focus photography. MSI measurements are captured by illuminating bubbles in a plane (or beam) offset from the focal plane of the camera. When in focus, the light scattered by a bubble that enters the camera lens is brought back down to appear as though it were a point source on the camera sensor. As the focal plane of the camera is moved slightly beyond the illumination plane this point appears to grow in size. As the distance between the focal plane and illumination plane increases this spot continues to grow in size and in standard photography the lens bokeh becomes visible. Its shape is determined by the internal aperture of the lens but is generally circular in shape producing bright ‘discs’ in an image. When monochromatic, coherent light is used to illuminate bubbles a portion of the aforementioned interference patterns is captured within this out-of-focus disc.

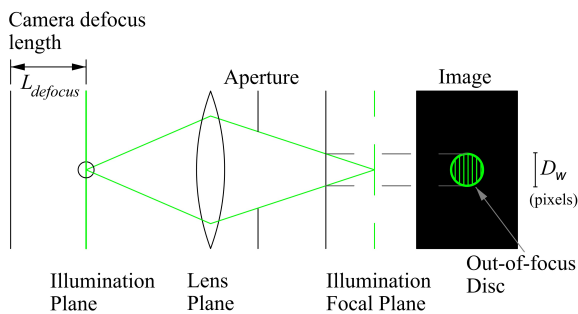


Fig. 1 A schematic showing the measurement principle of MSI. The technique measures interference fringes by capturing images that are out-of-focus from the illumination plane. Most lenses have a circular aperture so that light scattered from a particle forms a disc on the sensor, containing frequency information related to the particle size.

MSI is therefore based on Lorenz-Mie Theory (LMT) which describes rigorously the scattering of light by a permeable sphere from a incident plane wave (Bohren and Huffman, 2008). Computation time increases with bubble size but can be approximated through Geometrical Optics (Hulst and van de Hulst, 1981). For bubble measurements these approximations have been shown to be valid for measurement angles of less than 80° between the light source and the sensor (Semidetnov and Tropea, 2003). Extensions to geometric optical approximations continue to be developed (Sentis et al., 2016), to enable the use of this method for larger angles. However, for MSI measurements based on mapping of the interference fringe frequency to a diameter the extended

time for calculation is not an issue so that full Lorenz-Mie Theory can be used. Some implementations propose improvements in precision by using least-square-fitting of the interference pattern to theory (Graßmann and Peters, 2004). However, this method is very sensitive to the experimental parameters, and uncertainty in their measurement at larger working distances can negate the improvement in precision.

MSI was initially developed for application in droplet spray measurements, particularly in fuels (König et al., 1986; Skippon and Tagaki, 1996; Mounaim-Rousselle and Pajot, 1999). Since then various modifications to the technique have been developed. A cylindrical lens can be incorporated to compress interference patterns in one dimension on the sensor (Masanobu et al., 2000; Kobayashi et al., 2000; Qieni et al., 2014). This reduces overlap of the fringes when multiple particles/bubbles are present and thus increases the concentration limit of the technique. The use of laser light also lends itself to simultaneous particle-image velocimetry and size measurement (Kawaguchi and Maeda, 2005; Pu, 2005; Sahu et al., 2014). Novel methods have also been proposed to measure the 3D location of droplets in addition to the diameter through an optical arrangement that shears the interference pattern as the distance away from the sensing plane increases (Brunel and Shen, 2013; Shen et al., 2013). Despite these extensions, calibration of the technique for use in hydrodynamic test facilities remains a challenge, and experimental measurements comparing MSI to other techniques exhibit differences in the size distributions (Quérel et al., 2010; Ebert et al., 2015; Boucheron et al., 2018; Birvalski and van Rijsbergen, 2018). Calibration in a cavitation tunnel using electrolysis to create bubbles approximately half the diameter of the wire found unexpected bubble sizes in the measurements (Lacagnina et al., 2011), and it was suggested that systematic calibration take place outside the main facility to identify the source of these errors and reduce uncertainties. At the core of the problem are the uncertainties in mapping the interference pattern measured by the camera to the precise angular range this represents. This is exacerbated when working over large distances such as in hydrodynamic test facilities. In this regard, the most detailed treatment of sensitivity and uncertainty analysis for the bubble sizing calibration process has been by Dehaeck and van Beeck (2007), where the measurement of experimental parameters such as the location of lens or sensor planes are attributed the largest source of error and uncertainty in these calibration experiments. Custom lenses or specialist optics knowledge can provide the required precision (Mées et al., 2010), but for a standard multi-element lens and cameras such data may not be acces-

sible. Dehaeck and van Beeck (2007) examine multiple methods for calibration both theoretical and experimental, but note that direct experimental calibrations are hampered by the availability of mono-disperse bubble generators. From this work it is clear that should experimental calibration outside the main facility take place, there may be difficulty in replicating the same optical configuration that will be used in the primary facility, affecting the calibration.

In addition to the challenges in calibrating bubble size, the effective measurement volume must be ascertained in order to convert size distributions into bubble concentrations. This correction is not widely discussed in literature but is critical as the small measurement volume of MSI changes with bubble size (Mées et al., 2010). A theoretical method to calculate the size dependent detection volume has been adapted from the Laser-Doppler Velocimetry technique (Ebert, 2015), and greatly alters the measured bubble concentration distribution (Ebert et al., 2016). Due to its sensitivity, errors in the volume correction may account for some of the discrepancies between measurement techniques reported in hydrodynamic test facilities (Lacagnina et al., 2011; Mées et al., 2010; Ebert et al., 2015).

In this work we present a method to calibrate bubble size measurements for an MSI measurement system that uses commercially available camera and lens components for application in hydrodynamic test facilities. This application relates to cavitation nuclei where populations are typically in the size range 10 to 100 μm at volumetric concentrations of 0.01 to 10 mL^{-1} . This is conducted in a separate bubble chamber with identical optical characteristics to the primary facility to accommodate simultaneous shadowgraphy measurements used to validate the sizing calibration and afford greater control over sources of error. However, the calibration procedure itself may be conducted *in-situ* in the primary test facility and offers minor, yet important, improvements over alternative size calibration methods, circumventing a number of the uncertainties identified by Dehaeck and van Beeck (2007). In addition this work improves methods in determining the effective measurement volume of the technique. A mono-disperse bubble generator was used to produce bubbles of consistent size and an apparatus developed to modify inter-bubble spacing and control the positioning of bubbles within the MSI measurement volume. With this, the effective measurement volume with bubble size was explored experimentally. From these results improvements are made to the volumetric correction proposed by Ebert (2015); Ebert et al. (2016) and a calibration method for the size dependent measurement volume based on the location of bubbles in an MSI image is presented. In

principle this would enable use of an arbitrary shaped beam but uncertainties are reduced if the beam shape is close to Gaussian in profile.

The following section presents a summary of Lorenz Mie Theory and its approximations. The theory's implications for the measurement of bubbles in hydrodynamic test facilities are also discussed. We then demonstrate a method to produce mono-disperse microbubbles at concentrations suitable for measurement with both shadowgraphy and MSI in Sec. 3. This is accompanied by an experimental procedure to simultaneously measure a single microbubble with both techniques. This is used to rigorously calibrate MSI measurements (Sec. 4) and identify the detection volume (Sec. 5). Multiple frequency based MSI processing methods are discussed along with their implications for calibration. Uncertainties in both shadowgraphy and MSI are explored and MSI results are compared with theory.

2 Lorenz-Mie Theory

Although a conceptual understanding of the processes involved in the measurement technique does not require detailed knowledge of the mathematics behind Lorenz-Mie Theory, the selection of the scattering angle, collection angle, and the sampled scattered light polarization are assisted by connecting them to the theory. In addition, theory is often posed so that the coordinate system is defined independently of the incident light polarisation. While this abstraction is useful for analysis when the incident beam may be unpolarised, for highly polarised laser light this definition can cause confusion and obfuscate the choice of sampled scattered light polarization. A rigorous derivation of the far field intensity of light scattered by a bubble is provided by Bohren and Huffman (2008), the key components of which we will reproduce with minor changes to discuss the selection of parameters for measuring bubbles with polarised laser light.

Laser light propagates along the X axis and interacts with a bubble located at the origin (Fig. 2). The scattered intensity of light lobes in a complex pattern radiating outward to be captured by a camera. The angle between the beam and the vector from the bubble center to the middle of the camera lens is termed the scattering angle, θ . The plane created by these two vectors forms the scattering plane. Deviating from the standard approach, we define the angle between the plane of polarisation of the laser and the scattering plane to be the polarisation angle, ϕ . We now seek to calculate the intensity of scattered light for any values of θ and ϕ , which will have a component polarised parallel to the scattering plane ($E_{s||}$) and a component

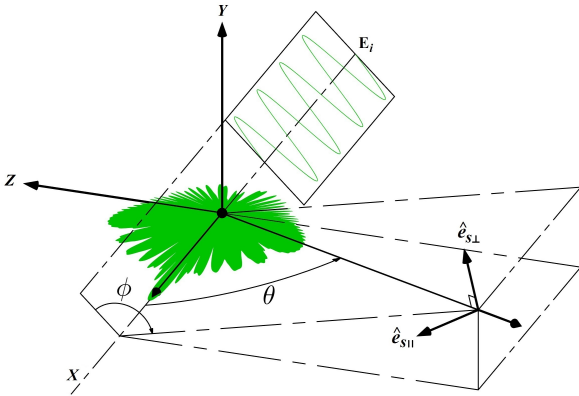


Fig. 2 Angular scattering of light from a bubble illuminated by a 532 nm plane wave propagating along the X-axis (E_i). The scattering angle, θ , is the angle between the illumination source and the viewing direction. Logarithmic intensity variations with scattering angle are shown for a sample plane in green.

normal to the scattering plane ($E_{s\perp}$). The range of θ in the scattering plane over which we measure intensity with our lens will be labelled α , our collection angle.

The dimensionless parameter, χ , describes the size of the bubble relative to the wavelength of light (λ) illuminating it and m is the ratio of the refractive indices of the two media, n_a and n_w for air and water, respectively.

$$\chi = \frac{2\pi n_w r}{\lambda} \quad m = \frac{n_a}{n_w} \quad (1)$$

These parameters dictate the overall spacing between interference lobes of the scattered light and at which scattering angle they appear. If the particle was non-spherical or required treatment with complex refractive indices the calculations would be more elaborate, but in the ideal case the theory for a single bubble is summarised with the equation

$$\begin{bmatrix} E_{s||} \\ E_{s\perp} \end{bmatrix} = E_i \frac{e^{ip}}{-ip} \begin{bmatrix} S_2(\theta) & 0 \\ 0 & S_1(\theta) \end{bmatrix} \begin{bmatrix} \cos(\phi) \\ -\sin(\phi) \end{bmatrix}, \quad (2)$$

where

$$S_1 = \sum_{n=1}^{\infty} \frac{2n+1}{n(n+1)} (a_n(\chi, m)\pi_n(\theta) + b_n(\chi, m)\tau_n(\theta))$$

$$S_2 = \sum_{n=1}^{\infty} \frac{2n+1}{n(n+1)} (a_n(\chi, m)\tau_n(\theta) + b_n(\chi, m)\pi_n(\theta)).$$

The scattering functions S_1 and S_2 are the truncated infinite sum of the scattering modes. They produce the intensity modulation the measurement technique utilises to size bubbles. It is observed from (2) that S_1 is associated with the light scattered from the bubble that is polarised perpendicular to the scattering plane, and S_2

parallel; this is not to be confused with the polarisation angle ϕ , although the relative intensity of S_1 and S_2 are a function of θ . The terms a_n and b_n comprise spherical Bessel functions, and the π_n and τ_n are constructed from associated Legendre polynomials. To investigate the components of these functions further does not enhance the discussion of the measurement parameters except to say that numerous computer codes exist to calculate numerically a_n , b_n , π_n and τ_n and we have used a particular MATLAB implementation by Mätzler (2002). It is however of interest to graph these scattering functions across a range of angles (Fig. 3) and point out some features.

For a 110 μm bubble the greatest contrast between the darkest and brightest part of the interference fringes is achieved at a scattering angle of approximately $10 < \theta < 45^\circ$ (Fig. 3a). However for a 10 μm bubble the fringe spacing is too large for a 10° collection angle, which is typically the upper limit for consumer lenses. The same problem occurs for $\theta > 120^\circ$ (Fig. 3b). A larger collection angle is then better as it limits the minimum detectable bubble size along with the measurement scattering angle. The design of custom lenses is of benefit (Lacagnina et al., 2011) but the specialist knowledge required may not be available to all hydrodynamic facilities. In any case, a region with high frequency oscillations is desirable as well as a lens with the largest collection angle. Fortunately, the measurement scattering angle of 90° lies in a region dense with fringes and is convenient for many experimental settings. While the selection of θ might be further optimised, angles other than 90° require a Scheimpflug lens arrangement to ensure the focal plane is parallel to the illumination plane, and may also introduce a working depth correction across the sensor (Quérel et al., 2010).

Comparing the two polarisations of scattered light for a 110 μm bubble in the region near 90° (Fig. 3b) the perpendicular S_1 component is brighter by an order of magnitude, and so would dominate the interference pattern if both components were present. However S_1 contains aberrant fringes resulting from surface effects (Pu, 2005; Sentis et al., 2016). These are seen in Fig. 3c at 87° , and 89° and less prominently at 91.5° and 93° . Later results show that their presence in the signal introduces greater uncertainty in size measurements as they degrade peak frequency extraction. However, S_2 alone can be measured by placing a polarising filter on the front of the camera lens. While the S_2 component has less variability in fringe wavelength, there is a rapid fall off in intensity across the region around 90° . To mitigate this, experimental data can first be de-trended by extracting frequency information from the residual of a linear fit to the data, keeping in mind that for

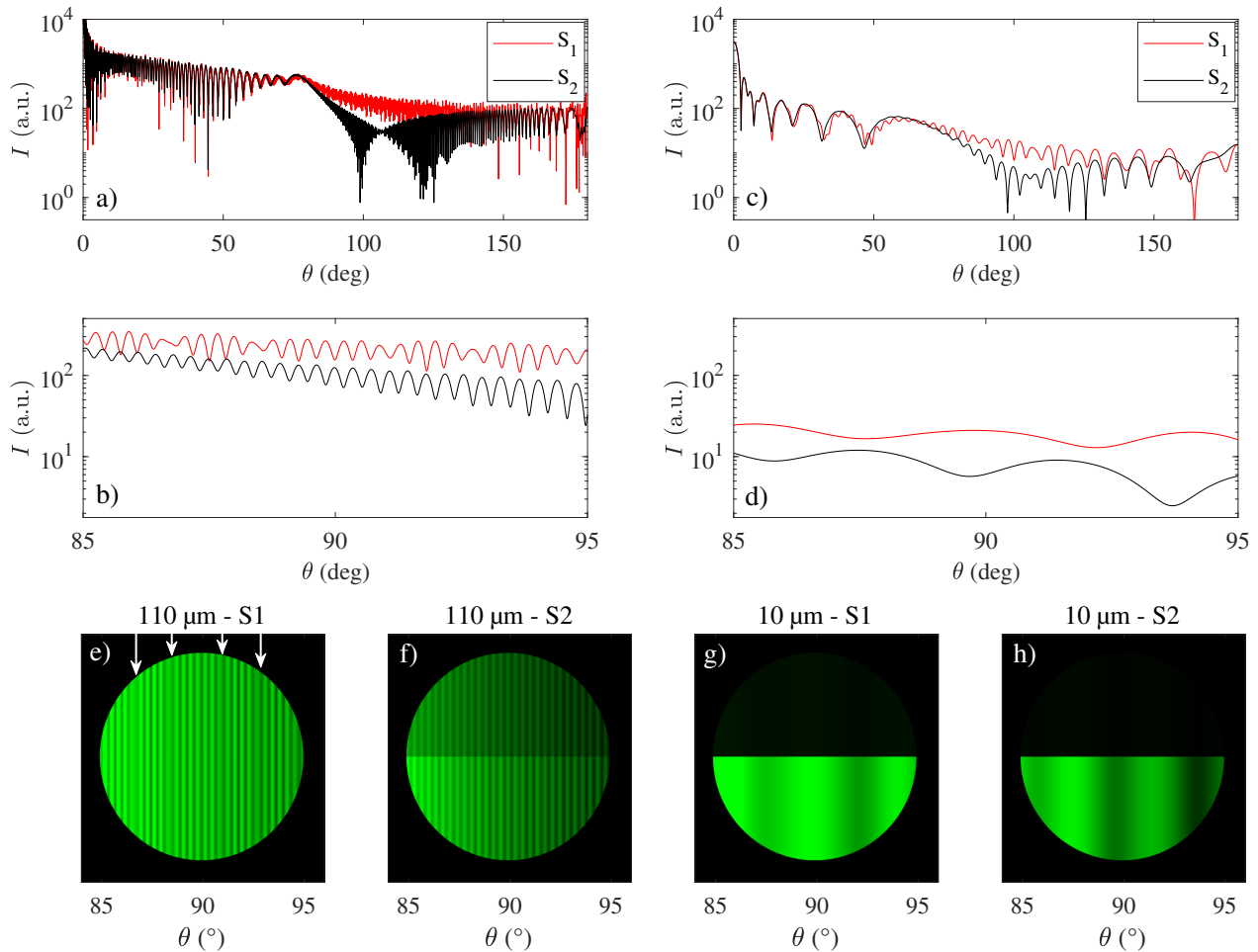


Fig. 3 Intensity of scattered light for an air bubble in water illuminated with 527 nm light. The S_1 (red) and S_2 (black) polarisations are given in the top two rows for microbubbles with diameter 110 μm (left) and 10 μm (right). The second row is restricted to $\pm 5^\circ$ about the viewing angle. The bottom row has synthetic images of the scattering pattern as captured by a circular aperture with a 10° collection angle. The aberrant fringes in the S_1 polarisation are indicated by the arrows. For the top half of each synthetic image the relative brightness is untouched. For the bottom half of each synthetic image the brightness has been normalised to make clear the frequency difference between sizes.

some measurements, one tail may drop into the noise floor of the camera sensor. The increased laser power requirements due to the decrease in scattered intensity of S_2 are usually inconsequential in most experimental settings. Clearly then we orient the laser to optimise measurement of the parallel polarisation. From Eqn 2 we can increase S_2 intensity and reduce S_1 by choosing $\phi = 0$. However, laser power is most stable when operating at maximum power. For lasers that are too bright at maximum power a polarising beam-splitter can be employed to dictate incident polarisation and reduce beam intensity.

LMT assumes a bubble is illuminated by an idealised plane wave of homogeneous intensity. Neither of these assumptions are strictly true. However for sufficiently small bubbles the scattering of light is not

greatly affected (Albrecht et al., 2013). This is limited to bubbles where the intensity of light does not deviate by 5% across the bubble area so that for a Gaussian beam the bubble diameter should be less than approximately 20% the beam width. Experimental results by Hesselbacher et al. (1991) indicate a less stringent requirement, for droplets at a scattering angle of 20° the diameter could be measured to an accuracy of better than 2% if the droplet diameter is smaller than the beam diameter. This describes an insensitivity in the interference pattern due to changes in illumination across the width of the microbubble, not the total intensity of light reflected and refracted by the bubble.

The mapping between the number of fringes N across an interference pattern and the bubble diameter can be derived from geometric optics in the case where

$20^\circ \leq \theta \leq 70^\circ$ as

$$d = \frac{2N\lambda}{\alpha} \left(\cos\left(\frac{\theta}{2}\right) + \frac{m \sin\left(\frac{\theta}{2}\right)}{\sqrt{m^2 - 2m \cos\left(\frac{\theta}{2}\right) + 1}} \right).$$

While inappropriate at $\theta = 90^\circ$, the mapping can still be approximated by a linear relationship with angular frequency (Boucheron et al., 2018). The most basic of which is posed as N , across measured collection angle α in Eq. 3a, but can also be expressed in terms of the angular wavelength of fringes λ_f as seen in Eq. 3b. The overbar in this context does not denote normalisation, as is the convention in quantum mechanics ($\bar{\lambda} \neq \lambda/2\pi$), but has been used to differentiate fringe wavelength from the wavelength of incident light. Experimental data will obtain the the wavelength in pixels λ_{px} which will be calibrated to an angular wavelength by C , an angular calibration constant the defocussed degrees per pixel.

$$d = \frac{KN}{\alpha} \quad \frac{[\mu\text{m}^\circ]}{[\circ]} \quad (3a)$$

$$= \frac{K}{\lambda_{deg}} \quad \frac{[\mu\text{m}^\circ]}{[\circ]} \quad (3b)$$

$$= \frac{K}{C \lambda_{px}} \quad \frac{[\mu\text{m}^\circ]}{[\circ \text{ px}^{-1}] [\text{px}]} \quad (3c)$$

As discussed by Boucheron et al. (2018) the value of K changes with the wavelength of the laser. To calculate K and assess if the method of processing will influence the measurement, a series of 4000 intensity curves for bubbles of $d = 10 - 200 \mu\text{m}$ with $\theta = 90^\circ$, and $\alpha = 5^\circ$ were generated. The overall trend line was subtracted to produce nominally zero-mean oscillations. Four methods were then used to extract the dominant wavelength: peak finding, auto-correlation, FFT, and wavelet analysis. Fig. 4a) shows a typical intensity series for a $100\mu\text{m}$ bubble. The detrended data is shown in red. The peak finding technique (Fig. 4b) used an inbuilt MATLAB algorithm to locate peaks of sufficient amplitude within the signal. The mean distance between the peaks was calculated to be the nominal wavelength. The second method used the first peak in the auto-correlation of the intensity series. (Fig. 4c) Sub-pixel resolution of the peak wavelength was achieved by fitting a spline to the seven points around the first peak and resampling at increased resolution. The third method (Fig. 4d) used a zero-padded FFT to increase the frequency resolution of the short series. The fourth method used wavelet analysis and a Morlet mother-wavelet to extract the dominant frequency by averaging the wavelength power across the interference pattern (Fig. 4f). Examples of the processing methods are shown in Fig 4a-f.

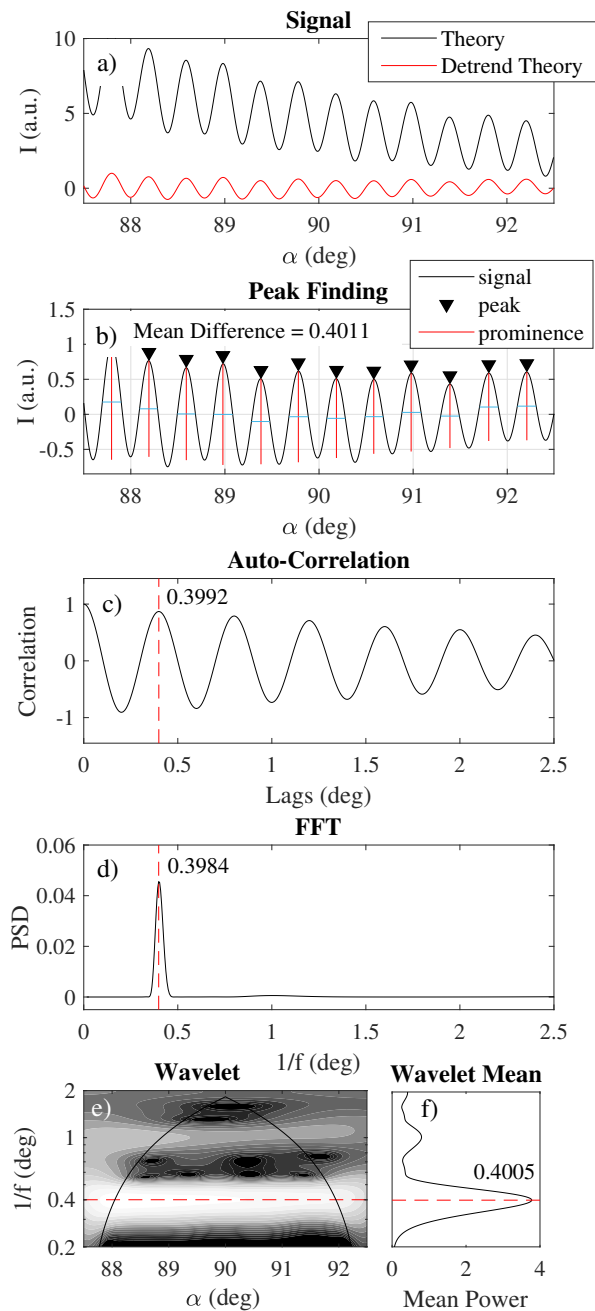


Fig. 4 The methods used to extract the fringe wavelength are applied to a theoretical intensity curve for a $d = 100 \mu\text{m}$ bubble.

The value of K was calculated with each method by rearranging Eq. 3b. This was prudent as our implementations produced different results (Fig. 5). All methods showed increased scatter in the calibrated K value at small diameters but in general the auto-correlation exhibited the least variation. This is in part attributed to the spline fitting method applied to this approach. Although this introduces an extra step in the computational process, the auto-correlation method remains

inexpensive to compute and reasonably insensitive to noise. Some fluctuation is inherent to K due to optical resonance inside the bubble (Damaschke et al., 2005). Whilst this represents a limitation for bubbles sizes less than about $30\mu\text{m}$, increasing the percentage uncertainty, overall this does not detract from the usefulness of the technique. As will be shown later in the results the uncertainty in measurements for bubbles $30\text{--}150\mu\text{m}$ remains about $1\mu\text{m}$.

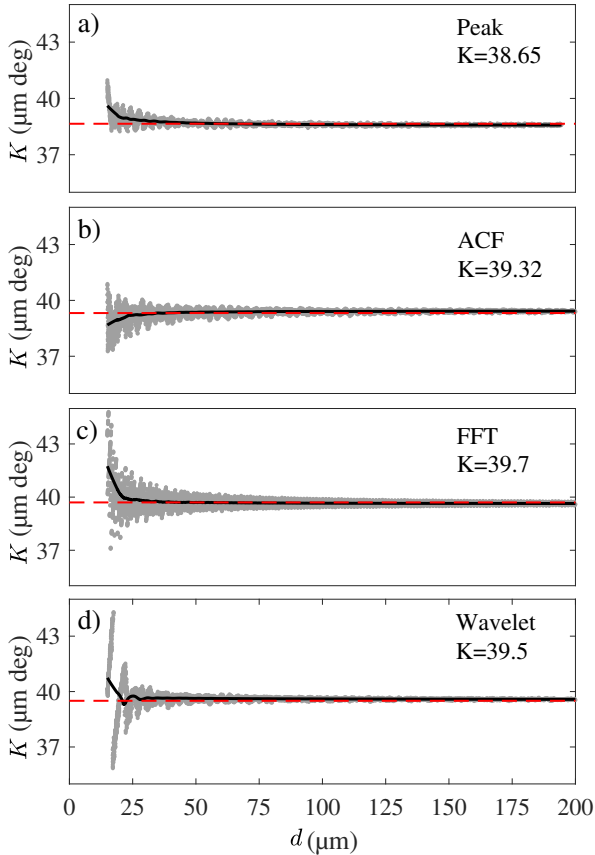


Fig. 5 The conversion factor K is plotted against the diameter as processed from the theoretical scattering intensity. Nominal conversion values are listed for each method.

3 Experiment Details

The experiment was performed in a 0.6 m square, 0.9 m long stainless steel test chamber. A schematic of the experimental setup is presented in Figure 6. Two optical tables were positioned either side of the test chamber, to which the cameras and laser equipment were mounted. In-line Long-range Microscopy Shadowgraphy (LMS) equipment was placed either side of the test chamber. Backlighting was provided by a LaVision high-efficiency diffuser attached to a Litron Nano

S 35-30-PIV Nd:YAG laser to produce a $4\ \mu\text{s}$ pulse of diffused $574\text{--}580\text{ nm}$ light. A BK7 glass port 79.5 mm thick allowed optical access for a LaVision Imager-LX PIV camera mounted behind a Questar QM100 long range microscope with a $2\times$ Barlow Lens to produce a magnification of $1.53\text{ pixels}/\mu\text{m}$. A custom nylon mount was manufactured so that a 62 mm polarising filter could be mounted to the end of the microscope objective to block the majority of light scattered by the bubble from the MSI laser which would otherwise be focussed onto the shadowgraphy CCD and potentially damage the camera sensor. Illumination for the MSI measurements was from a Litron Nano L 120-20-PIV 532 nm Nd:YAG laser. The beam was directed horizontally towards two Thorlabs NB1-K12 532 nm coated mirrors that redirected the light to 13.4° which finally passed through a Thorlabs CCM1-PBS25-532/M polarising beam splitter to control beam polarisation before entering the test chamber. The angle of 13.4° was set to provide beam access past the long range microscope and to avoid direct reflection on the measurement volume. The MSI beam passed through the same port used by the LMS receiving optics but low enough to ensure the light reflected by the glass port did not enter the long range microscope objective. A Nikon D850 DSLR with a Sigma 180 mm $1:2.8$ APO Macro DG HSM lens and a Promaster HGX Prime 86 mm polarised filter was used to capture MSI data. This was mounted with a Linos rail system to the end of the tank behind a second glass port to form a scattering angle of 90° . The camera was rotated 13.4° so that the horizontal pixel pitch was inline with the direction of the MSI laser.

Acquisition triggering was performed using a LaVision PCI 9 programmable timing unit run by Davis 8 for the shadowgraphy camera and both the MSI and shadowgraphy laser. The trigger pulse for the MSI laser was split to pass through a delay generator before connecting to the MSI DSLR camera. A wiring schematic is presented in Figure 7 and data was acquired at 0.5 Hz . The MSI laser was triggered $8\ \mu\text{s}$ after the shadowgraphy acquisition trigger to lower the risk of damage to the sensor but allow for simultaneous measurement of the bubbles by both techniques.

Monodisperse microbubbles for the comparison of the methods were produced by Lamylec-L10 $100\ \mu\text{m}$ and $50\ \mu\text{m}$ T-junctions from YLEC Consultants (Grenoble, France). These junctions accept pressurised air and water to generate a monodisperse train of bubbles from 30 to $130\ \mu\text{m}$ in size at a rate of $\sim 10^3$ bubbles per second. A Proportion-Air (QPV1TBNISZP10BRGAXL) electronic regulator with a Prevost $1\ \mu\text{m}$ air filter delivered pressurised air in the range of $0\text{--}10\text{ bar}$ to the junction. A second air regulator supplied pressure to

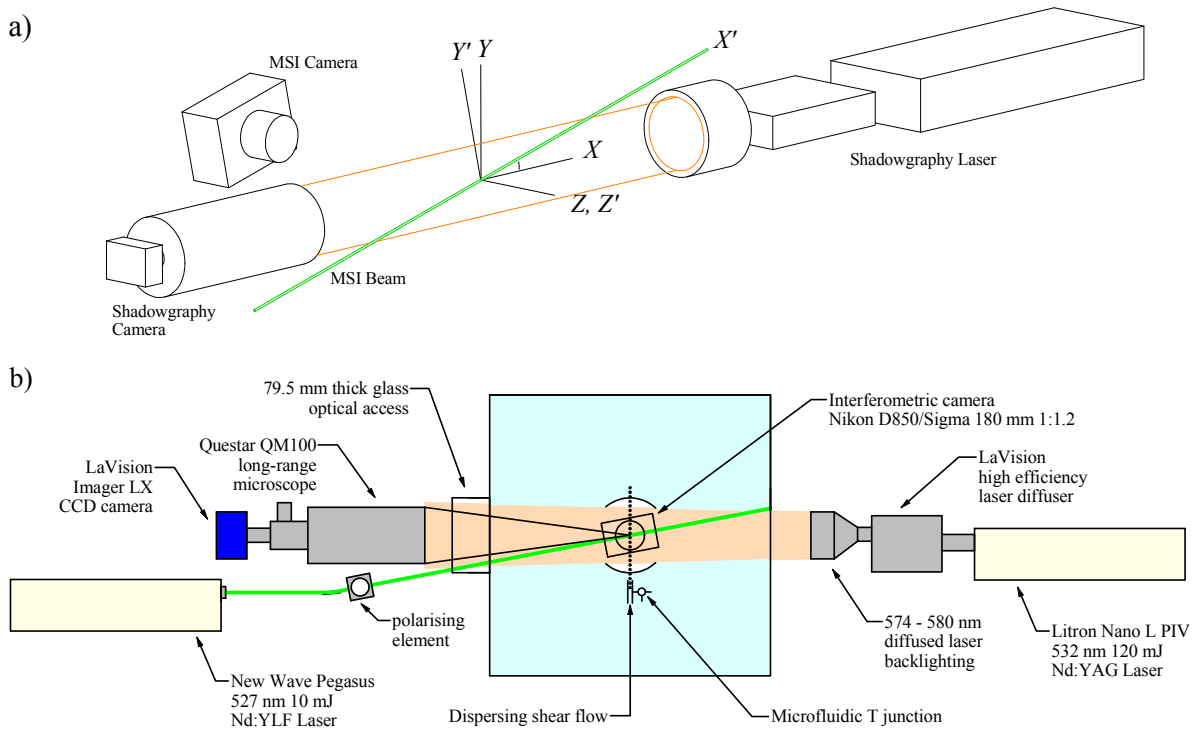


Fig. 6 a) Experiment coordinate system. MSI measurements are inclined by 13.36° to accommodate shadowgraphy measurements perpendicular to the glass wall window. b) Schematic in the XY plane, viewed from the positive Z direction with further experimental details.

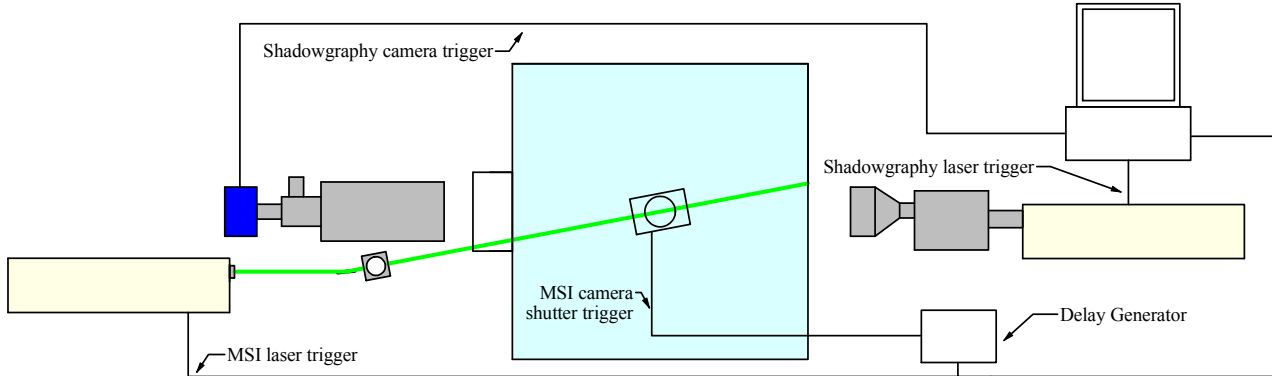


Fig. 7 Wiring diagram for triggering illumination and image acquisition equipment.

a water reservoir, the pressurised water was then supplied to the T-junction. Typical operating pressures are approximately 3 bar for both supply fluids. To produce sufficient spacing between bubbles the train was fed into a circular laminar cross flow 1 mm in diameter. The laminar cross flow was induced by water flowing under gravity from a constant-head tank positioned above the main chamber. The water level in the head tank was kept constant by a miniature centrifugal RS-Components 702-6876 pump, with excess water returned via an overflow line to main chamber. The cross flow jet was ejected vertically at a velocity of ~ 1 m/s into a

quiescent tank, with the measurement location approximately 30 mm above the jet outlet. If the cross flow was too fast the bubbles would not enter the core of the cross flow and travel more slowly near the passage walls where coalescence may occur. If the cross flow was too slow the bubbles may not be spaced appropriately. A schematic of the bubble generation and dispersion method is shown in Fig. 6(b). The T-junction and cross flow outlet were mounted to an acrylic arm. Precise 3D positioning of the arm was possible through three Melles-Griot 25 mm linear stage micrometers attached

between the arm and its mounting position outside the tank.

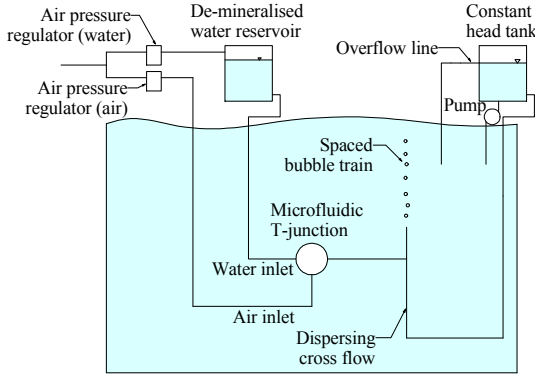


Fig. 8 Schematic of the bubble generation and dispersion apparatus.

The shadowgraphy measurements were acquired and processed using DaVis 8. To calibrate magnification factor and bubble sizing parameters in the LaVision system the acrylic arm and bubble generator was removed and brought into focus on a glass calibration plate supplied by LaVision, and placed in the center of the both optical access windows. Precise dots ($\pm 0.3 \mu\text{m}$) printed on the plate calibrated the magnification factor and bubble sizing parameters for the shadowgraphy measurements. The calibration plate has four dot sizes within the range of interest, that represent a nominal bubble diameter of 40, 60, 100, and $200 \mu\text{m}$. Zoomed sections of the calibration images are shown in Fig. 9a-d. Diffraction effects on the bubble edges are visible and their relative intensity is more noticeable on the smaller calibration dots. The pixel intensity was sampled horizontally through the center of the dot and plotted in Fig 9e. The effects of diffraction reduce the minimum pixel intensity and round the edges of the profile but otherwise agree well when normalised by minimum intensity and nominal bubble radius, measured with the DaVis Shadowgraphy package (Fig 9f). The histogram of dot diameters measured using optimised parameters from the calibration plate are shown in Fig 9g. The spread of the measured dot diameters around the known size gives an uncertainty estimate of $\pm 2 \mu\text{m}$ for the shadowgraphy measurement.

The MSI laser was then aligned to intersect the same location on the calibration plate. The bubble generation apparatus was then returned and positioned to be in focus for the shadowgraphy measurements. To confirm that the measurement volumes were coincident,

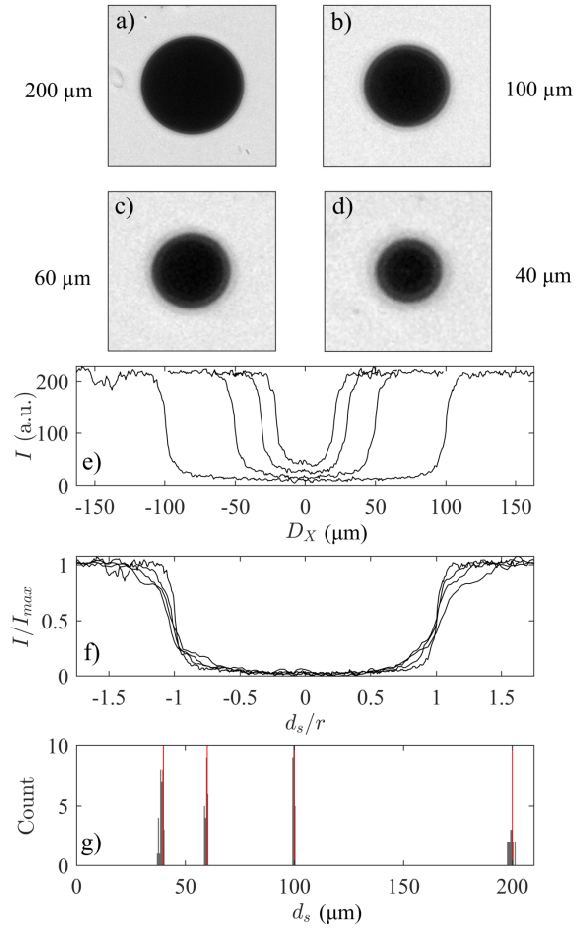


Fig. 9 A series of images and plots showing the calibration of the shadowgraphy images from a glass reference plate. Four example calibration dots of different size are extracted at different levels of zoom (a-d). Pixel intensity across dot center are plotted e). Normalised pixel series (f). Histogram of measured dot diameters for the calibration plate are presented (g).

the polarisation filter was removed from the shadowgraphy microscope objective and in simultaneous MSI and shadowgraphy measurements, with the MSI laser at low power, back scattered light from the MSI laser was observed using the shadowgraphy camera (Fig. 10). The depth of focus of the shadowgraphy equipment was small so that although focussed at the mid-plane of the bubbles, the backscattered light from front of the bubble is slightly out of focus. To measure the defocus distance of the MSI system a target plate was traversed from the bubble plane to the MSI camera focal plane using an electronic linear microstage. The uncertainty on the measurement of the defocus distance was $\pm 0.25 \text{ mm}$.

To capture a data set the air and water supply to the bubble generators were configured to produce the

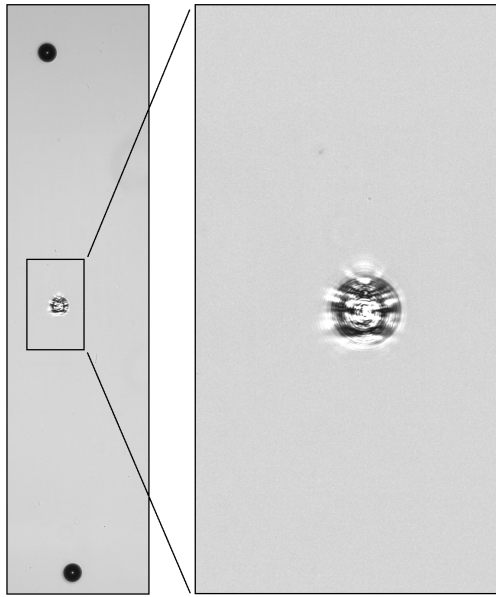


Fig. 10 Sample shadowgraphy image showing three 109 μm bubbles in the train. With the polarisation filter removed from the shadowgraphy camera, the MSI laser backscatter from the middle bubble is imaged, validating direct simultaneous measurement.

bubbles of the desired size. Sample shadowgraphy data was examined for a period of 5 minutes to assess bubble size spread and inter-bubble spacing. When appropriate bubble size and spacing characteristics were achieved 100 simultaneous MSI and shadowgraphy image pairs were captured. Figure 11 displays a typical shadowgraphy and MSI pair.

4 MSI calibration and Results

The polarising filter in front of the MSI camera could be adjusted to capture either the perpendicular or parallel polarised components of the light scatter by a bubble. The different features predicted by theory in each polarisation of the scatter light, see Sec. 2, were experimentally validated in Fig. 12. These data confirmed that parallel polarised light has greater homogeneity in wavelength when decomposed so that there is less scatter in the measured wavelength with size. Fresnel diffraction about the limiting aperture was also observed which needed to be accounted for in calibration.

The defocus distance, and therefore defocus disc width, was varied by moving the camera and lens together on a linear rail. It can be seen from Fig. 13 that the interference pattern can be normalised for a single bubble size by the interference disc width. The per-

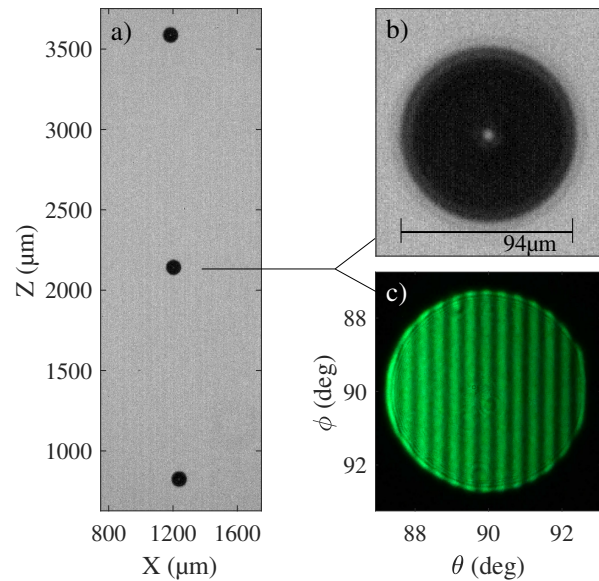


Fig. 11 Sample shadowgraphy and MSI picture pair for a 94 μm bubble. The magnified region shows the same bubble that is illuminated in the MSI picture.

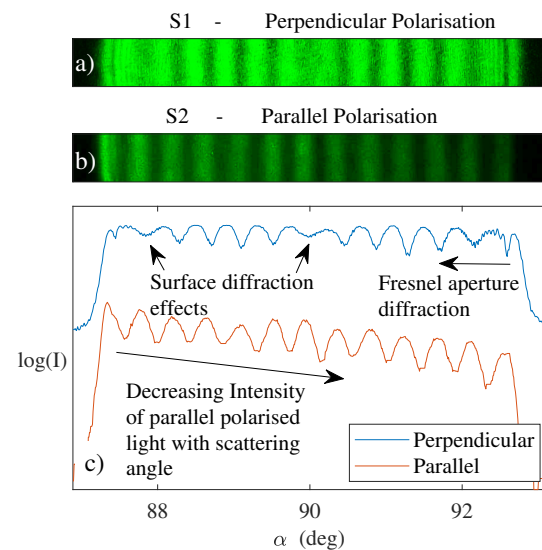


Fig. 12 MSI images for both S_1 (perpendicular, a) and S_2 (parallel, b) polarized light. The average intensity is given in (c), showing that S_2 is in general darker but has a more consistent wavelength across the collection angle.

pendicular polarisation was chosen for these measurements so that the presence of aberrant fringes were visible to help distinguish one fringe from its neighbour. The size of the defocus disc sets the maximum bubble size as the Nyquist limit is reached for the number of pixels per fringe wavelength. A competing requirement is that larger interference discs are more likely to overlap and so the measurable concentration limit decreases with disc size. The choice of disc size is then a function of the size and concentration ranges present.

While perhaps undesirable it will be shown that post measurement calibration of the technique is possible so that the defocus distance can be varied until the concentration is measurable by the system. A large bubble with fringe frequencies beyond the Nyquist limit may be erroneously sized as a much smaller bubble due to aliasing. The brighter intensity can be used to discriminate these bubbles (Ebert, 2015; Ebert et al., 2016). However, at the edge of a beam where the laser intensity reduces, such a bubble may be incorrectly accepted. In practical flows, these bubbles are few, as size distributions typically follow a negative power law (Russell et al., 2019), so that from a statistical standpoint they do not greatly bias results.

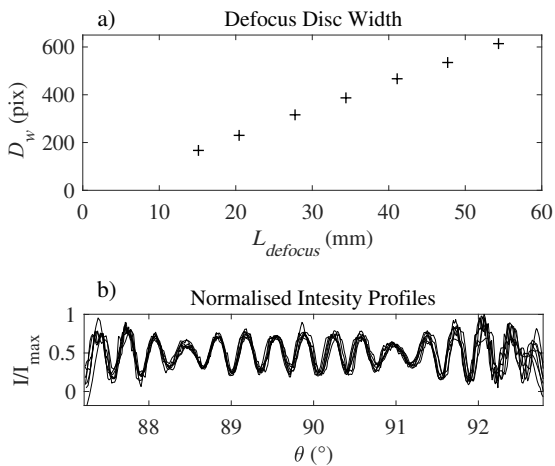


Fig. 13 The interference disc size in pixels (N_{pix}) as a function of the off-focus distance ($L_{defocus}$) of the camera and lens combined (top). Below, the normalised intensity profiles for perpendicularly polarised light are plotted showing an invariant profile with defocus distance.

To calibrate MSI there needs to be a mapping from the interference pattern in pixels to the angular scattering region this represents. One common approach is to measure the collection angle α , and observation/scattering angle and infer the region of measurement (Graßmann and Peters, 2004). In standard camera lenses the precise diameter of the limiting aperture is unknown and cannot easily be measured. In order to determine α accurately a new aperture whose width could be precisely measured was placed in between the bubble and the camera to mask the interference pattern. The width of the interference pattern in pixels then corresponds with the collection angle centered over the principle scattering angle of the camera. For bubble measurements it is advantageous that this aperture is located in the water so that the exact refractive index of the water, and more importantly glass, need not be known.

However, the measurement of the interference pattern width in pixels directly is prone to error (Dehaeck and van Beeck, 2007). Diffraction around the aperture edge in conjunction with the same intensity oscillations we wish to measure make resolving the true location of the geometric edge difficult. This can be circumvented by measuring the height of the interference pattern, but resolving the location of the geometric edge still posed a problem.

From Fresnel diffraction theory the intensity level at the geometric boundary location is 1/4 the unperturbed maximum intensity (Fig. 14). A rectangular aperture was placed in the test chamber and three vertical series were extracted from a sample image to measure the height in pixels and are compared in Fig. 14. One from the brightest part of a fringe, one from a dark band of the fringes, and the third series was constructed by taking the mean intensity across the image sample. The location of the edge, defined as the 1/4 maximum intensity, agreed well but the bright and dark pixels series are subject to pixel noise so that the mean intensity series was preferred. This method was then applied to a sample of 160 interference patterns. The histogram of results showed a spread of interference pattern widths (see Fig. 15).

An alternative method was implemented in order to avoid the need to find a geometric edge. Instead diffraction was used to our advantage. Two holes were machined in a thin plate which was then placed in the path between the camera and the bubble, (see Fig 16), similar to the limiting aperture method above. Aside from the geometry of the ‘aperture’ the only difference was now that the radial symmetry of the holes caused diffraction to create a series of concentric rings with a bright or dark spot in its center (Fig. 17). The distance in pixels between circle centers was able to be more accurately measured than locating the diffracted geometric edge. The calibration constant C was then calculated by,

$$C = \frac{\alpha}{D_{pix}} = \frac{2 \arctan(\frac{O}{A})}{D_{pix}}, \quad (4)$$

where O is the half distance of the aperture width, A the distance from the bubble to the limiting aperture, and D_{pix} the spacing between circle centers. Results for three aperture locations are tabulated below and agree well (Tab. 1).

With both measurement systems calibrated, the pressure of the air and water supplied to the T-Junction was varied to produce single bubble measurements ranging from ≈ 30 – $140 \mu\text{m}$ in diameter. The diameter measured by both techniques are plotted against one another in Fig. 18. The difference in measurements varied by less

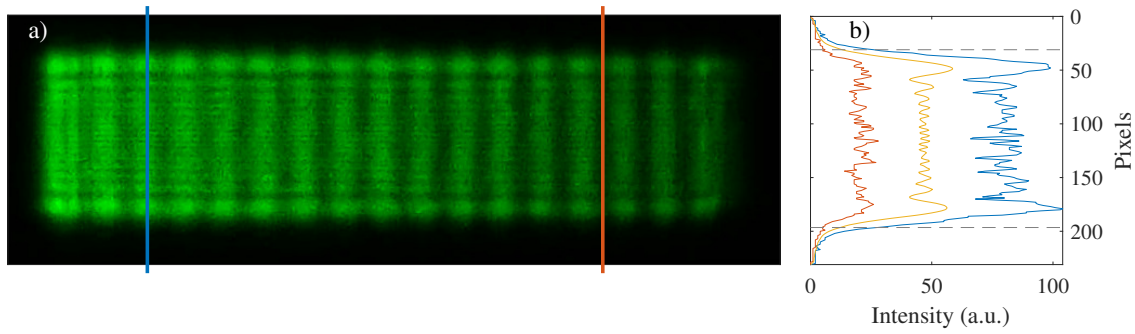


Fig. 14 (a) An interference pattern for scattered light clipped by a rectangular aperture placed in the water between the bubble and the camera lens. (b) Vertical intensity profiles are plotted for the blue and orange locations in a) as well as the horizontal mean intensity (yellow).

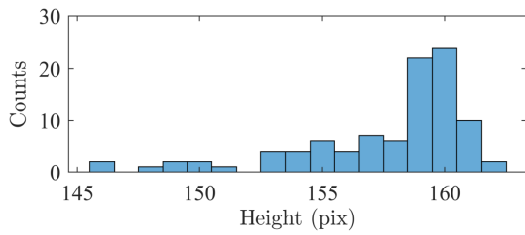


Fig. 15 A Histogram of measured interference heights for 160 sample images using the method from Fig. 14

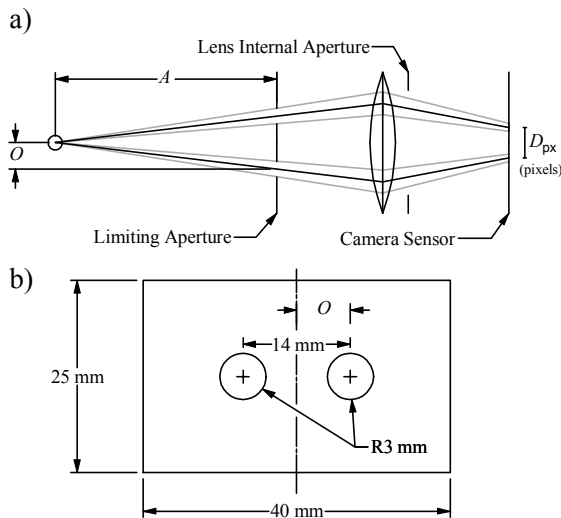


Fig. 16 (a) A schematic of the optical arrangement for the angular calibration. O is the half distance between the apertures, and A is the distance between the bubble and the mask plate. (b) The mask plate used in the angular calibration.

than $1 \mu\text{m}$. This gives confidence in the methods of calibrating and calculating the constants C and K , particularly as these were accomplished using separate information. It would otherwise be easy in calibration for the bias of one constant to propagate into the other, as discussed by Dehaeck and van Beeck (2007). From the

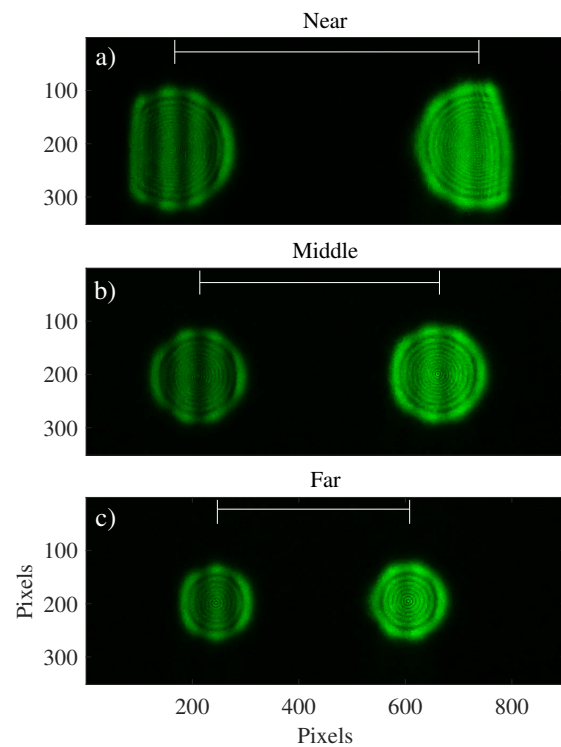


Fig. 17 Calibration images taken at three different distances (A in Fig. 16). The angle is reduced between the two apertures as the plate is moved farther from the bubble train.

theoretical calculation and plotting of K with size in Fig 5 there is greater uncertainty in K for small diameters. Further, there are fewer fringes across a single measurement so that there is greater uncertainty in the fringe wavelength. Uncertainty estimates for two bubble sizes are presented in Tab. 3. The uncertainty in C is constant and taken from Tab. 2. For small bubbles uncertainty in the measured fringe wavelength was estimated to be to within 1 pixels. For larger bubbles where many fringes can be sampled averaging allows for a sub pixel estimate of uncertainty. Linearised estimates of uncer-

Table 1 Calculations for calibration constant C for three distances from the bubble plume, presented also as $1/C$ for readability.

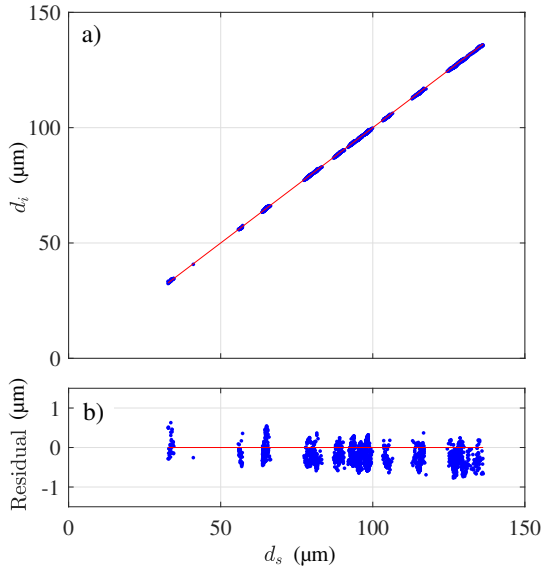
	$D_{aperture}$ (mm)	α_{holes} ($^{\circ}$)	D_{pix} (pix)	C ($^{\circ}/\text{pix}$)	$1/C$ ($\text{pix}/^{\circ}$)
Near	181	4.43	570.5	776e-5	128.8
Middle	229	3.50	450.0	778e-5	128.5
Far	285	2.81	360.5	780e-5	128.1

Table 2 Linearised estimate of the uncertainty in the calculated calibration constant C . The notation U_x is defined as the uncertainty in variable x

x	units	x_{est}	U_x	$ \frac{\partial C}{\partial x} \times U_x $	$\%U$
A	(mm)	181	± 0.5	3.39×10^{-5}	48.1%
D_{pix}	(px)	360.5	± 1	3.41×10^{-5}	48.7%
O	(mm)	7	± 0.005	8.77×10^{-6}	3.2%
U_C (total)				4.89×10^{-5}	($^{\circ}/\text{pix}$)

Table 3 Linearised estimate of the uncertainty in the calculated diameter for a 10 and 110 μm bubble. The notation U_x is defined as the uncertainty in variable x

10 μm					
x	units	x_{est}	U_x	$ \frac{\partial d}{\partial x} \times U_x $	$\%U$
K	($\mu\text{m deg}$)	39.32	± 2	0.499 μm	98.3%
C	($^{\circ}/\text{px} \times 10^{-5}$)	778	± 4.89	0.062 μm	1.5%
λ_{px}	(px)	515	± 1	0.019 μm	0.2%
U_d (total)				0.503 μm	
110 μm					
x	units	x_{est}	U_x	$ \frac{\partial d}{\partial x} \times U_x $	$\%U$
K	($\mu\text{m deg}$)	39.32	± 0.22	0.617 μm	16.5%
C	($^{\circ}/\text{px} \times 10^{-5}$)	778	± 4.89	0.693 μm	20.8%
λ_{px}	(px)	45.8	± 0.5	1.204 μm	62.7%
U_d (total)				1.52 μm	

**Fig. 18** (a) The size measured with MSI (d_i) is plotted against the size measured with shadowgraphy (d_s). (b) The residual ($d_i - d_s$) is plotted below with less than $1\mu\text{m}$ difference between the measurements.

tainty in d indicate that for small bubbles uncertainty in K dominates. For $d = 110 \mu\text{m}$ the primary uncertainty is the wavelength measurement, though the contribution of each variable to the overall total uncertainty in diameter are more evenly distributed. In any case, the shadowgraphy measurement uncertainty of $2 \mu\text{m}$ is bigger for both sizes. The minimum detectable bubble size (d_{min}) will depend on the collection angle of the system. As an optimistic estimate of the minimum bubble requires 1.5 fringe cycles across an interference pattern to attempt correlation. From equation 3a) and a collection

angle $\alpha \approx 5.5^{\circ}$ this corresponds to $d_{min} = 10 \mu\text{m}$. Practical limits are likely higher as smaller bubbles demonstrate increased scatter in K in this region. The largest detectable bubble is limited by either saturation of the image sensor, by the Nyquist criterion when the number of wavelengths is half the number of pixels across an interference pattern, or when bubble become aspherical at sizes above $200 \mu\text{m}$ in diameter.

5 Volumetric Concentration

To accurately calculate bubble concentration the measurement volume for each bubble size must be determined. The intensity of an MSI interference pattern is proportional to the intensity of incoming light as well as the 2D projected area of the bubble. Consequently, a large bubble may receive enough illumination across the full beam width to be measured, whereas a smaller bubble might only be recorded when in a narrow region at the center of the beam, Ebert et al. (2016). To examine this problem in detail bubbles were measured at various locations in the YZ plane, a cross-section of the MSI beam (See Fig.6a).

Bubbles were imaged with both shadowgraphy and MSI as they rose through the measurement volume. They were randomly located in the Y direction and systematically varied in the Z direction using a micro stage. The intensity of an interference pattern was defined to be the 95 percentile of the pixel series data (Fig. 19). A series of 1000 images was recorded for four bubble sizes and the jet outlet moved in $5 \mu\text{m}$ increments along the Z axis. The interference pattern intensity for one bubble size has been plotted as a function of position in Fig. 20a. The beam profile after passing through the chamber was expanded and captured using

a DSLR camera, shown for reference in Fig. 20b. Before testing the beam profile emitted from the laser head was measured with a Gentec-EO Beamage-4M beam profiler and produced a radially symmetric with a close to Gaussian profile. Beam optics and the angle at which the MSI beam entered the test chamber have clearly modified this beam shape. This may have implications for MSI configurations at angles other than $\theta = 90^\circ$. None-the-less, data in Fig. 20a compares well to the reference beam measurement Fig. 20b. In the future the beam will enter perpendicular to the glass port, but could not in this experiment without interfering with the shadowgraphy equipment. Whilst the shadowgraphy could be used to measure the effective beam width, a method that uses the measured beam profile and MSI data alone is outlined and validated using the available measurements.

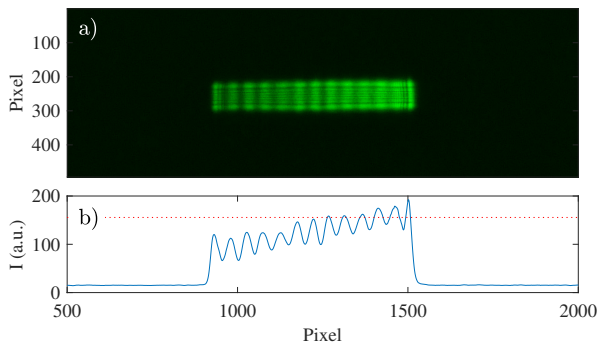


Fig. 19 a) Example interference pattern. b) Extracted pixel series. The red line indicates the 95th percentile, taken to be the representative intensity of the interference pattern.

For a practical measurement a beam-profiler can be placed at the same optical path length as the measurement volume from the laser head. The profile does not need to be Gaussian in shape. The centroid of an interference pattern in an MSI photograph can be related to its location in the beam (Fig. 21). The lens geometry and defocus distance will determine the magnification factor of an image at the illumination plane. Movement of the centroid in an image is mapped to its location across one dimension of the beam profile. With a large number of images, bubbles in a narrow size range can be interrogated to estimate the location at which the scattered light intensity is below the cut-off ($Y_{crit}(d)$). The maximum intensity across the beam profile at Y_{crit} can then be determined. A contour of the beam profile at this intensity value determines the effective beam area and the subsequent measurement volume. Note that this is only strictly true for a homogeneous flow, although the approximation should be very close.

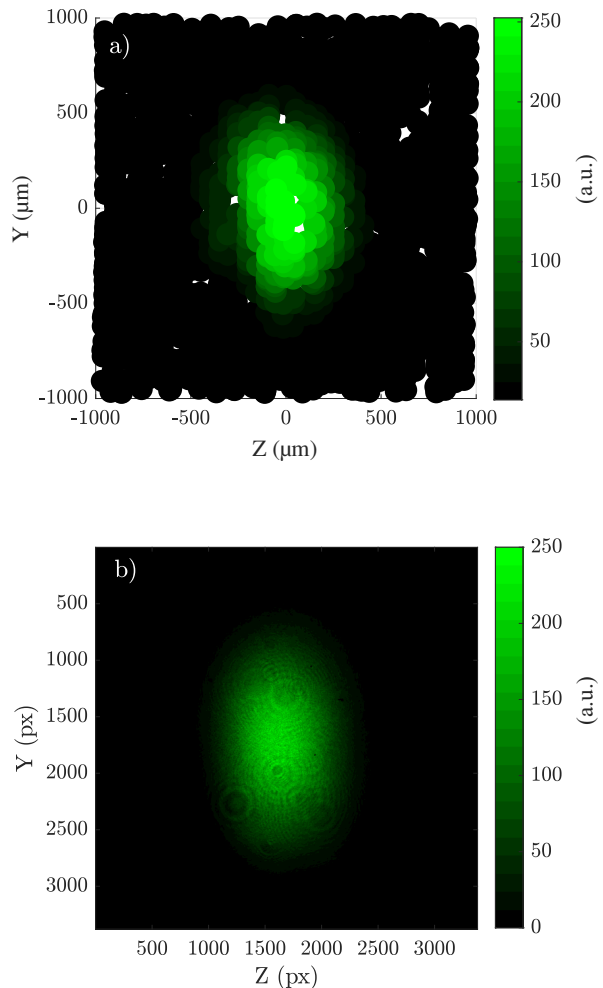


Fig. 20 a) Intensity of the scattered MSI light as a function of the spatial position of the bubble. b) Expanded beam profile.

To validate the approach we compare results using this method to data with the location known through shadowgraphy. First the Y location for MSI interference patterns are calculated from 2D cross-correlation of a rectangle template the same dimensions as the interference pattern with MSI photographs. Maxima of the cross-correlation identify bubble locations and are scaled by the magnification factor at the beam plane. Bubbles located via shadowgraphy are mapped to the MSI image and the intensity extracted. The Y -location and intensity are plotted for data extracted via MSI alone and shadowgraphy in Fig. 22. The two methods compare well and a sample fit is plotted for the shadowgraphy data. This process was repeated for four bubble sizes. A plot of the intensity profiles extracted from MSI data along with a fit to the data are presented in Fig. 23. An arbitrary minimum intensity threshold was set to be $I_{min} = 50$, which has also been plotted as a red dotted line in the figure. Contours for the location of

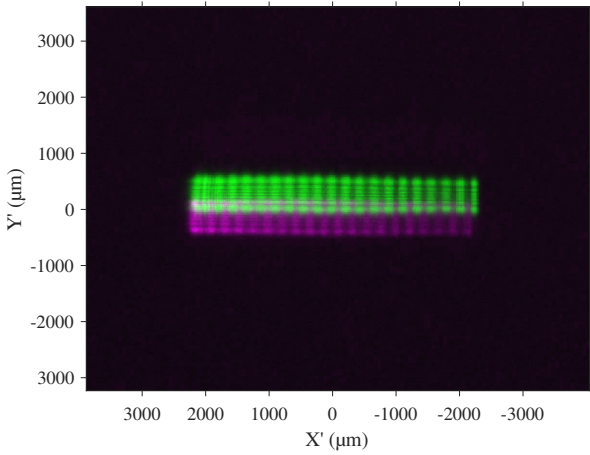


Fig. 21 Two MSI images superimposed demonstrate the shift in interference pattern as the location of the bubble varies within the MSI beam.

I_{min} for each of the bubble sizes are plotted in Fig. 24. These data are summarised as the effective beam width and beam area in Fig. 25.

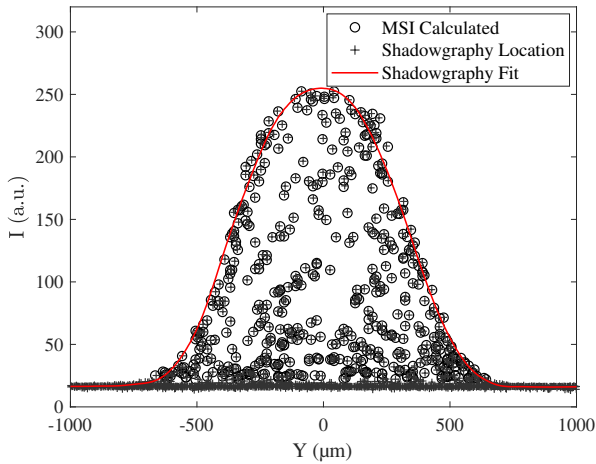


Fig. 22 A plot of Y -location against interference pattern intensity comparing the shadowgraphy and MSI methods.

6 Conclusions

The MSI technique has been investigated using simultaneous shadow imaging of individual mono-disperse microbubbles. The use of parallel polarisation was chosen instead of perpendicular at 90° scattering angle giving more uniform fringe spacing yielding greater precision despite the lower intensity. Calibration of the imaged fringe pattern was derived from two constants. The constant of proportionality between the scattering bubble diameter and the angular wavelength was determined from Lorentz Mie theory. A practical calibration for the

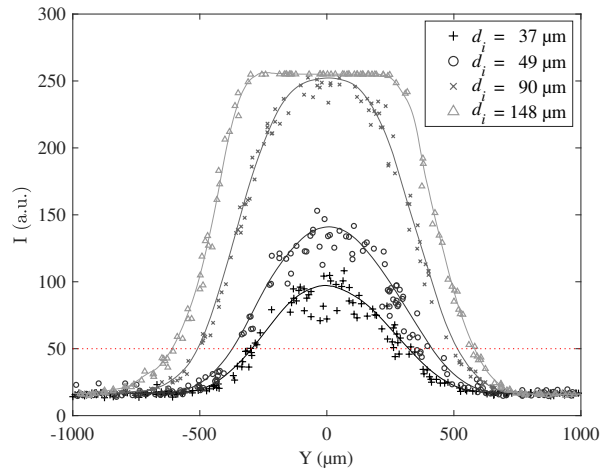


Fig. 23 Intensity profiles for four bubble sizes along the Y axis at $Z = 0$. The best fit surface for the intensity map is also plotted in solid lines for this cross section of the profile.

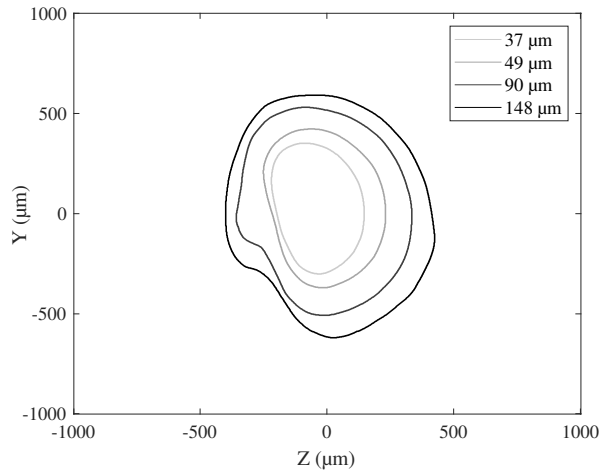


Fig. 24 Contours of for each bubble size of the beam area above the cutoff threshold.

second constant of proportionality between the scattering angle and imaged length is demonstrated. The comparison of the measured diameters by shadow and MSI by this approach within the range 30–150 μm is less than 1 μm . The diameter dependant effective measurement volume can be determined from the measured ensemble population if the beam profile is axisymmetric, or for an arbitrary beam shape if the profile is measured independently. A rationalised approach for the application of the MSI technique in water tunnels or other hydrodynamic test facilities using conventional laser diagnostic equipment is demonstrated. Although bubbles below 30 μm were not tested the method is applicable to sizes below 10 μm but with increased uncertainty. The approach is applicable for sparse concentration ranges, where interference pattern do not significantly overlap in images, to measure microbubbles in the diameter range 10–175 μm .

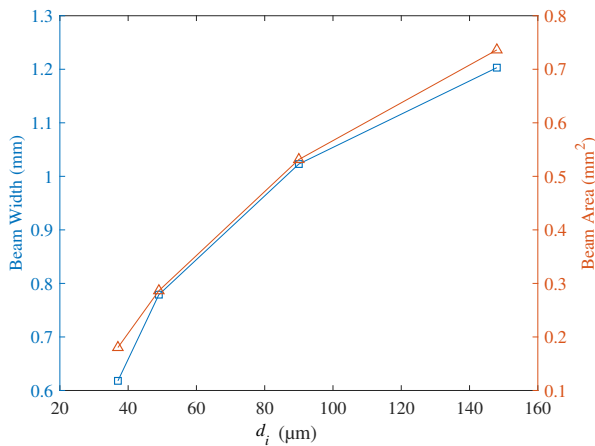


Fig. 25 The effective beam diameter and area are plotted against bubble diameter for four bubble sizes.

Acknowledgements This project was supported by the Defence Science and Technology Group (Dr. Dev Ranmuthugala and Mr. Matthew Khoo), the University of Tasmania, and the US Office of Naval Research (Dr. Ki-Han Kim, Program Officer) and ONR Global (Dr. Pae Wu) through NICOP S&T Grant no. N62909-15-1-2019.

References

- Albrecht HE, Damaschke N, Borys M, Tropea C (2013) Laser Doppler and phase Doppler measurement techniques. Springer Science & Business Media
- Birvalski M, van Rijsbergen MX (2018) Application of interferometric particle imaging to cavitation nuclei measurements in a ship model basin. In: Proceedings of the 19th 2018 International Symposium on the Application of Laser and Imaging Techniques to Fluid Mechanics, Lisbon
- Bohren CF, Huffman DR (2008) Absorption and scattering of light by small particles. John Wiley & Sons
- Boucheron R, Aumelas V, Donnet M, Fréchet D, Poizat A (2018) Comparative study of optical experimental methods for micro-bubble sizing. In: 19th International Symposium on Applications of Laser Techniques to Fluid mechanics, Lisbon, Portugal, p Paper 40
- Brandner PA (2018) Microbubbles and cavitation: Microscales to macroscales. In: Proceedings of the 10th International Symposium on Cavitation (CAV2018), ASME Press
- Brunel M, Shen H (2013) Design of ilids configurations for droplet characterization. *Particuology* 11(2):148–157, DOI <https://doi.org/10.1016/j.partic.2012.06.014>
- Chahine GL, Kalumuck KM (2003) Development of a near real-time instrument for nuclei measurement: the abs acoustic bubble spectrometer®. In: ASME/JSME 2003 4th Joint Fluids Summer Engineering Conference, American Society of Mechanical Engineers, pp 183–191
- Damaschke N, Nobach H, Tropea C (2002) Optical limits of particle concentration for multi-dimensional particle sizing techniques in fluid mechanics. *Experiments in Fluids* 32(2):143–152, DOI 10.1007/s00348-001-0371-x
- Damaschke N, Nobach H, Nonn TI, Semidetnov N, Tropea C (2005) Multi-dimensional particle sizing techniques. *Experiments in fluids* 39(2):336–350
- Deane GB, Stokes MD (2002) Scale dependence of bubble creation mechanisms in breaking waves. *Nature* 418(6900):839
- Dehaeck S, van Beeck JPAJ (2007) Designing a maximum precision interferometric particle imaging setup. *Experiments in Fluids* 42(5):767–781, DOI 10.1007/s00348-007-0286-2
- Dunker C, Roloff C, Grassmann A (2016) Interferometric laser imaging for in-flight cloud droplet sizing. *Measurement Science and Technology* 27(12):124,004
- Ebert E (2015) Optische messtechnik zur charakterisierung maritimer kavitationskeime. Thesis, Fakultät für Informatik und Elektrotechnik
- Ebert E, Kleinwächter A, Kostbade R, Damaschke N (2014) Interferometric particle imaging for particle characterization in the wake flow of a ferry ship and in cavitation tunnels. In: Proceedings of Lisbon 17th 2014 International Symposium On Applications of Laser Techniques to Fluid Mechanics, Lisbon
- Ebert E, Kröger W, Damaschke N (2015) Hydrodynamic nuclei concentration technique in cavitation research and comparison to phase-doppler measurements. *Journal of Physics: Conference Series* 656(1):012,111
- Ebert E, Kleinwächter A, Kostbade R, Damaschke N (2016) Hdnc - nuclei size and number concentration estimation with detection volume correction. In: 31st Symposium on Naval Hydrodynamics, Monterey, California
- Glover A, Skippon S, Boyle R (1995) Interferometric laser imaging for droplet sizing: a method for droplet-size measurement in sparse spray systems. *Applied Optics* 34(36):8409–8421
- Graßmann A, Peters F (2004) Size measurement of very small spherical particles by mie scattering imaging (msi). *Particle & Particle Systems Characterization* 21(5):379–389, DOI [doi:10.1002/ppsc.200400894](https://doi.org/10.1002/ppsc.200400894)
- Hesselbacher KH, Anders K, Frohn A (1991) Experimental investigation of gaussian beam effects on the accuracy of a droplet sizing method. *Applied Optics* 30(33):4930–4935, DOI 10.1364/AO.30.004930

- Hulst HC, van de Hulst HC (1981) Light scattering by small particles. Courier Corporation
- Katz J, Sheng J (2010) Applications of holography in fluid mechanics and particle dynamics. *Annual Review of Fluid Mechanics* 42:531–555
- Kawaguchi T, Maeda M (2005) Measurement technique for analysis in two-phase flows involving distributed size of droplets and bubble sizing using interferometric method - planar simultaneous measurement of size and velocity vector field. *Multiphase Science and Technology* 17(1-2):57–77, DOI 10.1615/MultScienTechn.v17.i1-2.40
- Kobayashi T, Kawaguchi T, Maeda M (2000) Measurement of spray flow by an improved interferometric laser imaging droplet sizing (ilids) system. In: 10th International Symposium on the Application of Laser Techniques to Fluid Mechanics, Lisbon, Portugal, paper, vol 10
- König G, Anders K, Frohn A (1986) A new light-scattering technique to measure the diameter of periodically generated moving droplets. *Journal of aerosol science* 17(2):157–167
- Lacagnina G, Grizzi S, Falchi M, Di Felice F, Romano GP (2011) Simultaneous size and velocity measurements of cavitating microbubbles using interferometric laser imaging. *Experiments in fluids* 50(4):1153–1167
- Masanobu M, Tatsuya K, Koichi H (2000) Novel interferometric measurement of size and velocity distributions of spherical particles in fluid flows. *Measurement Science and Technology* 11(12):L13
- Mätzler C (2002) Matlab functions for mie scattering and absorption, version 2. *IAP Res Rep* 8(1):9
- Mées L, Lebrun D, Allano D, Walle F, Lecoffre Y, Boucheron R, Fréchou D (2010) Development of interferometric techniques for nuclei size measurement in cavitation tunnel. In: Proceedings of the 28th Symposium on Naval Hydrodynamics
- Mounaïm-Rousselle C, Pajot O (1999) Droplet sizing by mie scattering interferometry in a spark ignition engine. *Particle & Particle Systems Characterization: Measurement and Description of Particle Properties and Behavior in Powders and Other Disperse Systems* 16(4):160–168
- Pu S (2005) Developpement de methodes interferometriques pour la caracterisation des champs de particules. Thesis, Rouen
- Qieni L, Xiang W, Tong L, Zhen L, Yimo Z (2014) Linear interferometric image processing for analysis of a particle in a volume. *Journal of Optics* 16(4):045,703
- Quérel A, Lemaitre P, Brunel M, Porcheron E, Gréhan G (2010) Real-time global interferometric laser imaging for the droplet sizing (ilids) algorithm for airborne research. *Measurement Science and Technology* 21(1):015,306
- Randolph K, Dierssen HM, Twardowski M, Cifuentes-Lorenzen A, Zappa CJ (2014) Optical measurements of small deeply penetrating bubble populations generated by breaking waves in the southern ocean. *Journal of Geophysical Research: Oceans* 119(2):757–776
- Russell PS, Barbaca L, Venning J, Pearce B, Brandner P (2019) Measurement of nuclei seeding in hydrodynamic test facilities. *Experiments in Fluids* (submitted for publication)
- Sahu S, Hardalupas Y, Taylor A (2014) Droplet-turbulence interaction in a confined polydispersed spray: effect of droplet size and flow length scales on spatial droplet-gas velocity correlations. *Journal of Fluid Mechanics* 741:98–138
- Semidetnov N, Tropea C (2003) Conversion relationships for multidimensional particle sizing techniques. *Measurement Science and Technology* 15(1):112
- Sentis MPL, Onofri FRA, Méés L, Radev S (2016) Scattering of light by large bubbles: Coupling of geometrical and physical optics approximations. *Journal of Quantitative Spectroscopy and Radiative Transfer* 170:8–18, DOI <https://doi.org/10.1016/j.jqsrt.2015.10.007>
- Shen H, Coetmellec S, Brunel M (2013) Simultaneous 3d location and size measurement of spherical bubbles using cylindrical interferometric out-of-focus imaging. *Journal of Quantitative Spectroscopy and Radiative Transfer* 131:153–159, DOI <https://doi.org/10.1016/j.jqsrt.2013.04.009>
- Skippon S, Tagaki Y (1996) Ilids measurements of the evaporation of fuel droplets during the intake and compression strokes in a firing lean burn engine. *SAE transactions* pp 1111–1126
- Venning J, Khoo M, Pearce B, Brandner P (2018) Background nuclei measurements and implications for cavitation inception in hydrodynamic test facilities. *Experiments in Fluids* 59(4):71
- Xu R (2001) Particle characterization: light scattering methods, vol 13. Springer Science & Business Media